Proceedings of the 7th International Symposium on Cavitation
CAV2009
August 17-22, 2009, Ann Arbor, Michigan, USA

CAV2009 – Paper No. 56

A Numerical Study of Unsteady Cavitation on A Hydrofoil

Sung-Eun Kim
Naval Surface Warfare Center Carderock Division
West Bethesda, MD, U.S.A.

ABSTRACT

The unsteady turbulent cavitation on a hydrofoil with finite span and NACA-0015 section is studied numerically. For the computations, a two-phase flow approach based on homogeneous mixture approximation is adopted in which liquid-vapor mixture is modeled as an inter-penetrating continuum with the phase compositions represented by volume-fraction and the inter-phase mass transfer computed using a finite-rate model derived from bubble dynamics. An implicit, finite-volume based projection algorithm was developed that couples velocity, phase compositions, and pressure. Turbulence is modeled using Reynolds-averaged Navier-Stokes (RANS), large eddy simulation, and RANS/LES hybrid approaches. A suite of multiphase computational fluid dynamics (MCFD) solvers was built using OpenFOAM, an object-oriented, open-source CFD tool-kit, being validated for steady and unsteady cavitating flows on hydrofoils and marine propulsors. The large eddy simulation (LES) and the RANS/LES hybrid results on the hydrofoil closely reproduced the salient features of the unsteady sheet/cloud cavitation such as the breakup of sheet cavity by re-entrant jet, and the formation and collapse of cloud cavity. The lift and drag force predictions in a range of cavitation number were also found to be in good agreement with the experimental data in terms of the mean values, the root-mean-square values, and the spectral contents.

INTRODUCTION

Cavitation is arguably one of the most challenging phenomena to numerically predict in fluid dynamics. Analogous to general multiphase flows well known for the presence of multiple regimes, the varying interfacial topology involved with cavitation, which appears in the form of bubbles, sheets, slugs, threads, and clouds of small bubbles, makes the numerical modeling of cavitation difficult. Adding to the complexity and difficulty of numerical modeling, cavitation encountered in industrial applications occurs in turbulent flows that carry a wide range of length and time scales. Clearly, interactions between turbulence and two-phase flow physics would be extremely very complex. Thus, turbulence modeling continues to be an important issue, yet far more challenging than in single phase turbulent flows.

Cavitation inception and early stage of bubbly cavitation are often approached by studying the behavior of discrete bubbles evolving in carrier fluid flows using Lagrangian bubble tracking and bubble dynamics equations (Chahine, 2004 [1]). Numerical prediction of fully developed cavitation such as sheet cavity, on the other hand, has favored continuum (Eulerian) approaches. The majority of the continuum approaches adopted for cavitation modeling are based on homogeneous mixture approximations in which vapor and liquid phases are modeled as an inter-penetrating mixture moving with the same velocity, and their compositions are determined by solving the volume-fraction transport equation (Merkle *et al*., 1998 [2]; Kunz *et al*., 1999 [3]; Singhal *et al*., 2002 [4], Senocak and Shyy, 2002 [5, 6]; Schnerr and Sauer, 2001 [7]; Wikstrom, 2003, 2005 [8, 9]). The mechanical equilibrium assumption underpinning the homogeneous continuum mixture theory largely holds true for both stratified flows with sharp interfaces and liquid flows laden with small bubbles.

Mathematical modeling of phase change occurring with cavitation is the centerpiece of the continuum mixture based approach in cavitation modeling. Several phase change models have been proposed (Merkle *et al*., 1998 [2]; Kunz *et al*., 1999 [3]; Singhal *et al*., 2002 [4]; Senocak and Shyy, 2004a [5], 2004b [6]; Schnerr and Sauer, 2001 [7]; Hosangadi and Ahuja, 2005 [10]. Despite heuristic arguments and *ad hoc* assumptions used in their derivations, these models have been shown to give reasonable predictions of some types of cavitation such as steady sheet cavity and vortex cavity. In a

slightly less popular approach, cavitating two-phase flows are represented as a density-varying single-phase flow using a barotropic relationship between pressure and density (Delannoy and Kueny, 1990 [11]; Song and He, 1998 [12]; Reboud *et al*., 1998 [13]; Coutier-Delgosha *et al*., 2007 [14]). This approach has been adopted by the group at the St. Anthony Falls Laboratory of the University of Minnesota who have been studying, for many years, unsteady sheet and cloud cavitation on a NACA-0015 hydrofoil, both experimentally and numerically (Song and He, 1998 [12]; Arndt *et al*., 2001 [15]; Qin *et al*., 2003 [16]).

The numerical methods employed by the earlier efforts are predominantly projection methods (Delannoy and Kueny, 1990 [11]; Kubota *et al*., 1992 [17]; Ventikos and Tzabrias, 2000 [18]; Singhal *et al*., 2002 [4]; Senocak and Shyy, 2002 [5]; Wikstrom, 2005 [9]. With these projection algorithms, one is often faced with numerical difficulties mainly caused by large difference in density, high rate of mass transfer, and lack of a closed form of state equation for the mixture that manifest in the form of solution instability or divergence.

This paper is concerned with an application of a high-fidelity multiphase computational fluid dynamics (MCFD) capability to the turbulent cavitating flow on a hydrofoil. As the computational framework, we adopted a two-phase approach based on the aforementioned homogeneous mixture approximation that is believed to have a high potential to describe the salient physics involved in various types of turbulent cavitating flows encountered in naval hydrodynamics. Inter-phase mass transfer is modeled using a finite-rate phase-change model derived from a simplified Rayleigh-Plesset equation in favor of its simplicity and ability to reflect the physics involved in vaporization and condensation processes.

An implicit, iterative projection algorithm was developed that tightly couples velocity, phase composition, and pressure using an outer iteration loop within each time step. The implicit solution algorithm was found to significantly increase the maximum allowable CFL number and, as a consequence, to greatly improve the solution stability. In the projection algorithm for the "compressible" mixture, the pressure equation was derived from the continuity equation written in an inhomogeneous divergence equation (Yuan and Schnerr, 2003 [19]; Wikstrom, 2005 [8]). Turbulence is modeled using Reynolds-averaged Navier-Stokes (RANS), large eddy simulation, and detached eddy simulation (DES) approaches. The two-phase flow solvers, the turbulence models, and the mass-transfer model were integrated into a suite of MCFD solvers using OpenFOAM, an object-oriented, open-source CFD tool-kit written in C++.

GOVERNING EQUATIONS

The governing equations for two-phase mixture flow adopted in this study are derived using a formalism based on the concepts of phase indicator and weighted averaging or filtering of the original Navier-Stokes equations (Ishii, 1975 [22]). Depending on the weighted averaging and filtering schemes adopted, the resulting equations take different forms that need to be interpreted accordingly and have implications to turbulence closure. We follow an approach that has been widely adopted by many others for modeling mixture flows.

The transport equation for volume-fraction of liquid phase (γ) can be written in a conservative form as:

$$\frac{\partial \gamma}{\partial t} + \nabla \cdot (\gamma \mathbf{u}) = \nabla \cdot \left(\frac{\nu_t}{\sigma_\gamma} \nabla \gamma \right) + \frac{\dot{m}}{\rho_\ell} \tag{1}$$

where $\mathbf{u}$ is the mixture velocity, and $\dot{m}$ is the rate of net mass transfer between vapor and liquid phases, and will be elaborated shortly. Note that the turbulent diffusion term is included in the equation.

The governing equations for the mixture flow-fields are a single set of averaged Navier-Stokes equations. The continuity (mass conservation) equation for the mixture is given by

$$\frac{\partial \rho}{\partial t} + \nabla \cdot (\rho \mathbf{u}) = 0 \tag{2}$$

Note that, for mixture flows with phase-change, divergence of the mixture velocity field does not vanish. Obviously, phase change between the vapor and the liquid phases gives rise to non-vanishing volume dilation ($\nabla \cdot \mathbf{u} \neq 0$).

The momentum equation can be written in the form:

$$\frac{\partial}{\partial t}(\rho \mathbf{u}) + \nabla \cdot (\rho \mathbf{u}\mathbf{u}) = \nabla \cdot \{ -p\mathbf{I} + \boldsymbol{\tau} \} + \rho \mathbf{g} \tag{3}$$

where the viscous/turbulent stress is determined from:

$$\boldsymbol{\tau} = \mu_{eff} \left(2\mathbf{S} - \frac{2}{3}\mathbf{I}(\nabla \cdot \mathbf{u}) \right)$$

and $\mu_{eff} = \mu + \mu_t$, with μ_{eff} is the effective viscosity, $\mathbf{g}$ the gravity. The mixture properties like density and dynamic viscosity are computed as functions of γ from

$$\begin{aligned} \rho &= \gamma \rho_\ell + (1-\gamma)\rho_\upsilon \\ \mu &= \gamma \mu_\ell + (1-\gamma)\mu_\upsilon \end{aligned} \tag{4}$$

where the subscripts "ℓ" and "υ" denote liquid and vapor, respectively.

From the expression for the mixture density in Eq. (4), the continuity equation can be rewritten in the form of inhomogeneous divergence equation as:

$$\nabla \cdot \mathbf{u} = -\frac{1}{\rho}\frac{d\rho}{dt} = \frac{\rho_\ell - \rho_\upsilon}{\rho}\frac{d\gamma}{dt} \tag{5}$$

From Eq. (1) and Eq. (5), the mass transfer rate, $\dot{m}$, can be shown to become

$$\dot{m} = \frac{\rho_\upsilon \rho_\ell}{\rho}\frac{d\gamma}{dt} \tag{6}$$

With this definition of $\dot{m}$, the continuity equation can be rewritten in terms of the mass transfer rate as:

$$\nabla \cdot \mathbf{u} = \dot{m}\left(\frac{1}{\rho_\ell} - \frac{1}{\rho_v}\right) \tag{7}$$

In summary, Equations (1), (3), and (7) are the ones that are actually solved as will be discussed later.

TURBULENCE MODELING

RANS, LES, and RANS/LES hybrid approaches are employed in this study. Modern RANS turbulence models widely used for single-phase flows have been demonstrated to be also able predict steady or quasi-steady cavitation such as attached sheet cavity and tip-vortex cavity with reasonable accuracy (Singhal *et al*., 2002 [4]; Senocak and Shyy, 2002 [5]). Much less has been demonstrated about whether RANS computation can predict highly transient sheet cavitation involving re-entrant jet, break-up of sheet cavity, and formation and collapse of cloud cavitation accompanied by violent vortex-shedding. It is deemed essential to explicitly resolve not only large scales of motion that RANS is considered able to capture to some extent but also smaller scales directly responsible for breaking up sheet cavity into smaller chunks and eventually into clouds of small bubbles. LES or RANS/LES hybrid approaches should help in this regard.

For the RANS computations carried out for this study, Wilcox' *k*-ω (Wilcox, 1998 [23]) and the realizable *k*-ε models (Shih *et al*., 1995 [24]) were used in their original forms without any modifications. For the LES computations, subgrid-scale (SGS) terms are modeled using Smagorinsky's eddy-viscosity model. The subgrid-scale stresses are written as

$$\boldsymbol{\tau} - \frac{1}{3}\mathbf{I}\, tr(\boldsymbol{\tau}) = -2\rho C_S \overline{\Delta}^2 \|\mathbf{S}\|\mathbf{S} \tag{8}$$

where C_S (= 0.1) is the model constant, $\mathbf{S}$ the resolved rate-of-strain tensor, and $\|\mathbf{S}\|$ its modulus.

For RANS/LES hybrid model computations, we adopted the original detached eddy simulation (DES) approach (Spalart *et al*., 1998 [25]).

MASS TRANSFER MODELING

We start by writing the volume-fraction of vapor phase as

$$1-\gamma = \frac{\frac{4}{3}\pi R_b{}^3 N_b}{1+\frac{4}{3}\pi R_b{}^3 N_b} \tag{9}$$

where N_b is the nuclei number density (the number of nuclei per unit volume), and R_b the bubble radius. Taking the derivative of Eq. (9), we get

$$\frac{d\gamma}{dt} = -\frac{3\gamma(1-\gamma)}{R_b}\frac{dR_b}{dt} \tag{10}$$

where R_b, can be written in terms of N_b as:

$$R_b = \left(\frac{3(1-\gamma)}{4\pi\gamma N_b}\right)^{1/3}$$

The rate of mass transfer can now be written as:

$$\dot{m} = -\frac{3\rho_v\rho_\ell}{\rho}\frac{\gamma(1-\gamma)}{R_b}\frac{dR_b}{dt} \tag{11}$$

With the simplified Rayleigh-Plesset (R-P) equation

$$\frac{dR_b}{dt} = sign(p_v - p)\sqrt{\frac{2|p-p_v|}{3\rho_\ell}} \tag{12}$$

the mass transfer rate can finally be written as:

$$\dot{m} = \frac{-3\rho_v\rho_\ell}{\rho}\frac{\gamma(1-\gamma)}{R_b}sign(p_v - p)\sqrt{\frac{2|p-p_v|}{3\rho_\ell}} \tag{13}$$

The expression in Eq. (13) was originally derived by Schnerr and Sauer (2001) [7]. Similar expressions were derived by several others using reduced forms of Rayleigh-Plesset's bubble dynamics equation. With this model, the mass transfer is mainly driven by the pressure differential, $|p-p_v|$. Note that the bubble number density (N_b) does not appear explicitly in Eq. (13), but is absorbed in the local bubble radius, R_b, which is a function of bubble number density and volume-fraction. Volume-fraction, bubble number density, and bubble radius, any two of which are independent parameters, also affect the mass transfer. Unlike some of the mass transfer models widely used today in which a user-specified time-scale is required (Merkle *et al.*, 1998 [2]; Kunz *et al.,* 1999 [3]), time-scale of the phase-change in this model is naturally accounted for via the simplified R-P equation which should be able to describe, at least, the physics involved in the early stage of cavity growth more closely than other heuristically derived models. Along with the transport equation for volume fraction, the non-equilibrium effects like history and transport effects are also accounted for by this model. What we thought is missing in the original Schnerr and Sauer's (S-S) model in Eq. (13) is a provision which can reflect the fact that the rates of vaporization and condensation could differ substantially. Thus, we slightly modified the original S-S model to accommodate the different rates of mass transfer, replacing Eq. (13) with

$$\dot{m} = \dot{m}_c + \dot{m}_v \tag{14}$$

where

$$\begin{aligned}
\dot{m}_c &= C_c\frac{3\rho_v\rho_\ell}{\rho}\frac{\gamma(1-\gamma)}{R_b}pos(p-p_v)\sqrt{\frac{2}{3}\frac{|p-p_v|}{\rho_\ell}} \\
\dot{m}_v &= -C_v\frac{3\rho_v\rho_\ell}{\rho}\frac{\gamma(1-\gamma)}{R_b}pos(p_v-p)\sqrt{\frac{2}{3}\frac{|p-p_v|}{\rho_\ell}}
\end{aligned} \tag{15}$$

where C_c and C_v are the rate constants ($\approx O(1)$) for condensation and vaporization, respectively, and the function

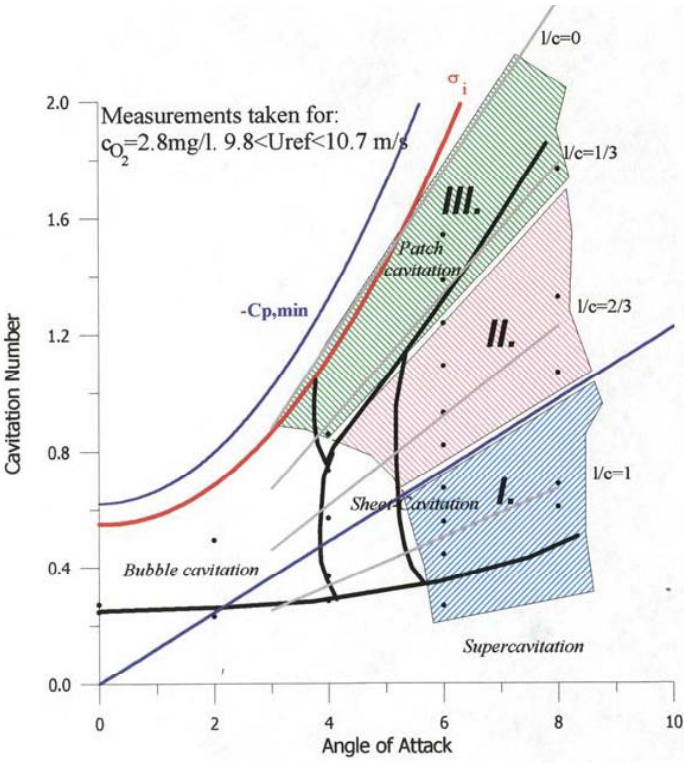

Figure 1. Cavitation regime map for NACA-0015 hydrofoil (Kjeldsen *et al.*, 2000. Taken from Ref. [21]).

"pos" is the Heaviside function defined by: $pos(x)=1$ when $x \geq 0$; $pos(x)=0$ otherwise. To close this model, bubble number density and initial bubble (nuclei) radius are needed. Bubble number density can simply be assumed to be given and constant. Alternatively, it can be determined from its transport equation with source terms to account for breakup and coalescence of bubbles. In this study, we took the first approach.

NUMERICAL METHOD

The CFD solvers in OpenFOAM employ a cell-centered finite-volume method based on a multi-dimensional linear reconstruction scheme that permits use of computational elements (cells) with arbitrary polyhedral cell topology including quadrilateral, hexahedral, triangular, tetrahedral, pyramidal, prismatic, and hybrid meshes. The solution gradients at cell centers can be evaluated by applying Green-Gauss theorem or by least-square method. For discretization of convection terms in the momentum and turbulence equations, we used the "filtered linear scheme" that is essentially a second-order-accurate central-differencing scheme with overshoot and undershoot in the solution fields locally filtered out.

For discretization of advection term in the volume-fraction transport equation, we employed the van Leer scheme. We decided not to use any special interface-capturing scheme widely adopted for stratified flows with sharp interfaces, since it was deemed not suited for two-phase cavitating flows involving phase change. The source term in the γ-equation was linearized using the usual technique widely used to linearize source terms in transport equations for positive transport variables.

A projection algorithm for velocity-pressure coupling has been developed for two-phase mixture flows involving mass transfer.

The momentum equations can be written in a semi-discrete form

$$a_P \mathbf{u}_P = \mathbf{H}(\mathbf{u}) - \nabla p \tag{16}$$

or equivalently,

$$\mathbf{u}_P = \frac{\mathbf{H}(\mathbf{u})}{a_P} - \frac{\nabla p}{a_P} \tag{17}$$

where a_P is the diagonal component of the coefficient matrix, and $\mathbf{H}(\mathbf{u})$ represents the non-diagonal terms and the source terms. Substituting Eq. (17) into the continuity equation, Eq. (7), and using the Green-Gauss theorem for the divergence yields

$$\nabla \cdot \left[\left(\frac{1}{a_P} \right)_f \nabla p \right] = \sum_f \left[\mathbf{S}_f \cdot \left(\frac{\mathbf{H}(\mathbf{u})}{a_P} \right)_f \right] - \dot{m} \left(\frac{1}{\rho_\ell} - \frac{1}{\rho_v} \right) \tag{18}$$

where the subscript "f" denotes the values at cell faces. The source term due to the mass transfer in this equation – the second term on the RHS of the equation - was linearized in p (pressure) by rearranging the expressions in Eq. (15). A similar linearization was used by Wikstrom (2005) [9] with the Kunz' (1999) mass transfer model.

The discretized governing equations are solved using point-implicit Gauss-Seidel relaxation along with an algebraic multi-grid (AMG) method to accelerate solution convergence. The MCFD solver suite can be run in parallel using domain decomposition and message passing with OpenMPI library.

PROBLEM DESCRIPTION

The subject flow was selected to represent the class of unsteady cavitating flows involving sheet and cloud cavities. This class of cavitating flows warrants an in-depth study for their high relevance to naval applications. However, the complex physics involved in these highly dynamic two-phase flows poses significant challenges to numerical modeling. Among several candidates, we picked the NACA-0015 hydrofoil, mainly because it has been studied in great detail, both experimentally and numerically, by several independent groups in different countries in the last two decades (Kubota,

1992 [17]; Arndt *et al*., 2001 [15]; Qin and Song, 2003 [16]; Hosangadi and Ahuja, 2005 [10]; Wang and Ostoja-Starzewski, 2007 [20]). As shown in Figure 1, the dynamics of the cavitation on this rather thick, symmetric hydrofoil varies greatly with the angle of attack and the cavitation number. We have been carrying out 2-D and 3-D computations with RANS, LES, and DES on the hydrofoil at an 8° angle of attack and at two cavitation numbers. According to the regime map in Figure 1 (Kjeldsen *et al*., 2000 [21]), under the conditions considered, the flow features sheet cavitation accompanied by shedding of cloud cavity as aptly illustrated in Figure 2. The Reynolds number considered was 1.0×10^6 which is slightly higher than the ones used in the earlier experiments (3.0×10^5 in Kubota *et al*., 1992 [17]; 7.0×10^5 in Arndt *et al*., 2001 [15]).

BOUNDARY, INITIAL CONDITIONS, AND OTHER COMPUTATIONAL DETAILS

Two computational meshes of a C-type, a 35,500-cell, structured mesh and a finer mesh with 288,000 cells were used for the 2-D RANS computations. The 3-D RANS, LES, and DES computations were mostly made on a 1.2 million-cell mesh obtained by extruding the coarse 2-D mesh in the span-wise direction by one chord-length. A separate LES run was made on a 3 million cell mesh to check the mesh dependency.

The domain boundary consists of the far-field boundary (freestream), the hydrofoil surface (wall), and the exit boundary. The domain extends 4.0 and 8.0 chord-lengths upstream and downstream of the foil, respectively. The lateral boundaries are placed at 5.0 chord-lengths from the hydrofoil centerline. The 3-D mesh has two additional boundaries created by the extrusion in the spanwise direction. The near-wall mesh resolution is such that $y^+ < 1$ along most of the hydrofoil surface.

On the upstream and the far-field boundaries, the freestream values of velocity components and volume-fraction are specified ($U = U_0 \cos\alpha$; $V = U_0 \sin\alpha$; $\gamma = 1.0$). On the exit (outlet) boundary, velocity and volume fraction are extrapolated. The static pressure was fixed on the exit boundary with the value that would give the desired cavitation number from:

$$\sigma \equiv \frac{p_{exit} - p_v}{\frac{1}{2}\rho_\ell U_0^2} \tag{19}$$

The computations were carried out for σ = 0.6, 0.8. 1.0, 1.2, and 1.5.

On the hydrofoil surface, we employed a two-layer wall-function approach that invokes proper wall-laws depending on the y^+ value at wall-adjacent cells, although the near-wall resolution adopted in this study never invoked the log-law.

A fixed dimensionless time-step size of 0.0002 (c/U_0) was used for all the computations. The time-step size was determined based on the estimates of the characteristic length and time scales of the eddy size to be resolved. The smallest time-scale to be resolved was computed from $\tau = \ell / u'$, where ℓ was taken as 0.01 c, and u' as $0.5U_0$. From these rough estimates, one turnover of the smallest resolved eddies will be resolved with roughly 100 time steps.

The parameters for the mass transfer model used in this study are: C_c=0.2, C_v=0.1, $N_b = 2\times10^7$, R_0 = 50 μm. The solutions were initiated from the freestream values with the mass transfer model deactivated until the flow-fields are largely established, typically for a period of 0.5 c/U_0. The mass transfer model was then turned on to allow the cavitation to occur.

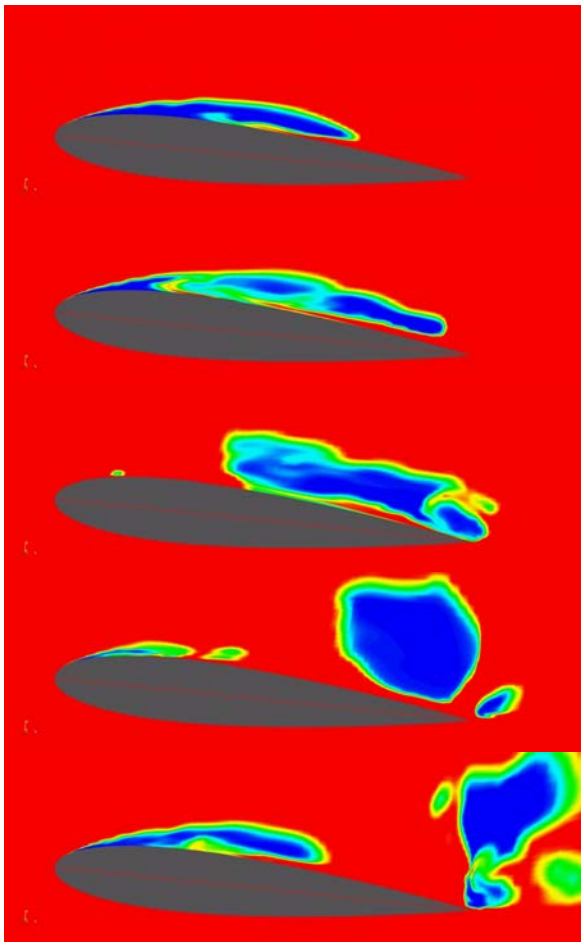

Figure 2. Evolution of the sheet/cloud cavity predicted on a NACA-0015 foil at α = 7° and σ = 1.0 using 2-D RANS with the realizable k-ε model on the coarse mesh.

The computations were mostly carried out on a Linux cluster using up to 24 CPU's at the SeaTech Center of the NSWCCD.

RESULTS

The 2-D RANS computations made using both Wilcox's k-ω turbulence model and the realizable k-ε model for non-cavitating flows at $\alpha = 7°$ on the two meshes of different resolution showed no noticeable sign of large-scale unsteadiness in the boundary layer. The only noticeable sign of (weak) unsteadiness was found in the near-wake, in the results on the finer mesh, where Kelvin-Helmholtz' waves were observed. However, the RANS computations at reduced cavitation numbers with the same turbulence model yielded drastically different flow patterns, predicting highly unsteady flow-field and cavitation dynamics. The 2-D RANS results obtained with the realizable k-ε model are illustrated in Figure 2. Interestingly enough, and as will transpire shortly, the 2-D RANS computations largely reproduce the gross features of the turbulent cavitating flow observed in water tunnels at the incidence angle and the cavitation number considered, such as the breakup of sheet cavity by the re-entrant jet, and the formation and what appears to be the collapse of cloud cavity. Despite the qualitative agreement, the major frequency of the sheet cavity oscillation and the shedding of the cloud cavity, which was clearly identifiable in the experimental data, was much less obvious and could not be determined with the 2-D RANS results, although animation of the 2-D RANS results showed quasi-periodic oscillations that seemingly repeat the sequence depicted in Figure 2.

Given the flow-field and cavitation predicted by the 2-D RANS computation, which was less coherent than the experiments suggest, it was concluded that, in order to address the dynamics involved in unsteady sheet/cloud cavitation in earnest, 3-D computations are in order. It was not clear, however, what level of turbulence modeling would be needed to accurately predict not only the flow and cavitation structures but also the lift, drag and the frequency content in the forces acting on the hydrofoil. Thus, 3-D computations were carried out on a relatively coarse 3-D mesh with RANS, LES, and DES approaches.

Figure 3 shows the snapshots of the instantaneous volume-fraction contours on a longitudinal 2-D cut through the mid-span (z/c = 0.5) for approximately one cycle of oscillation. Pure liquid ($\gamma = 1$) is shown in black, whereas pure vapor in white. The frame-to-frame time interval is 0.5 c/U_0.

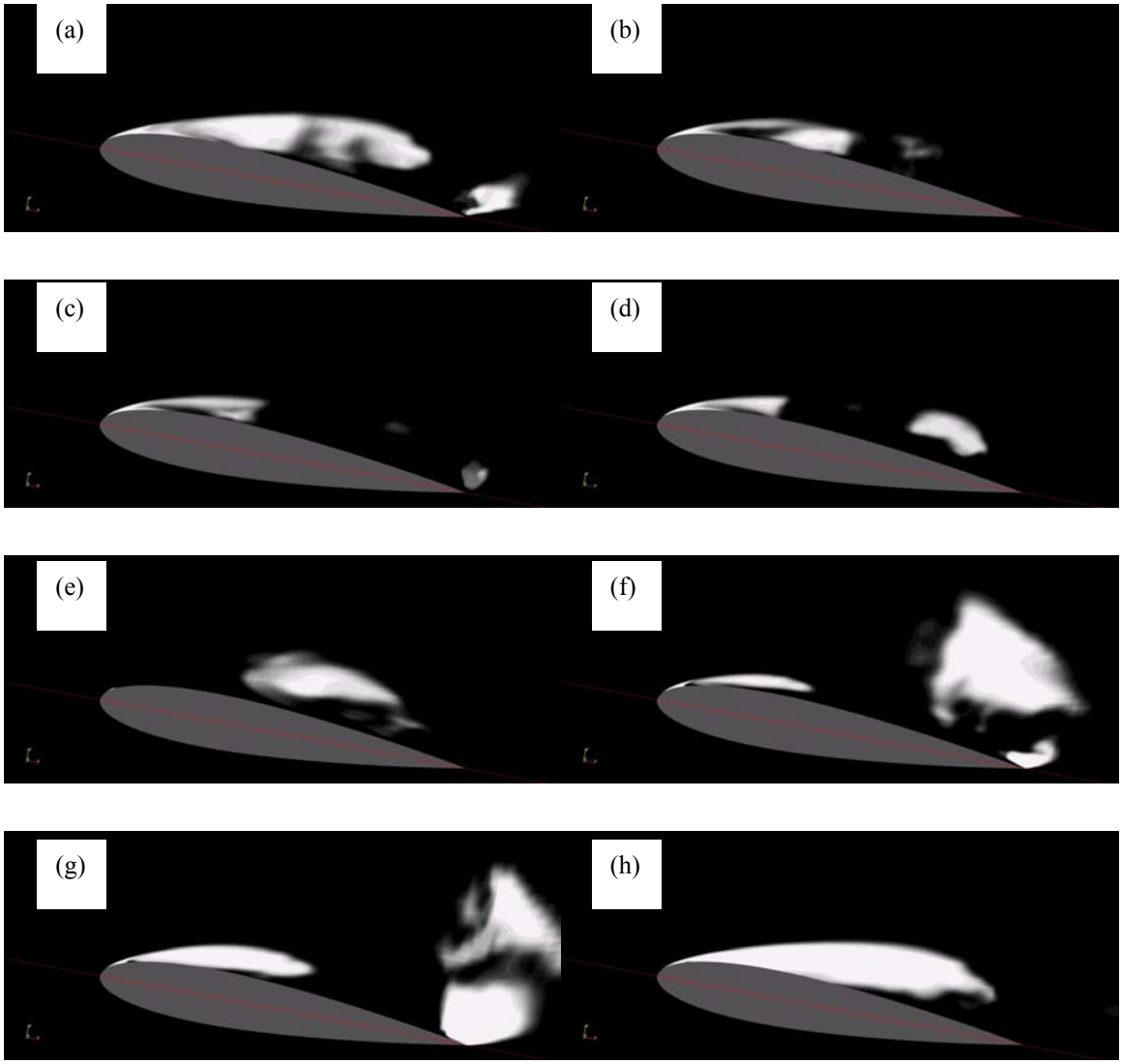

Figure 3. LES (3-D) results – contours of instantaneous volume-fraction on a longitudinal cut through the mid-span portraying the break-up of sheet cavity and the formation of cloud cavity and its shedding on NACA-0015 hydrofoil at $\alpha = 8°$ and $\sigma = 1.0$.

It should be kept in mind that the figures shown here are the snapshots of only a slice of a 3-D structure, and the figures show roughly only one cycle of events. Nonetheless, the sequence depicted in the figures portrays the sheet cavity broken up by the re-entrant jet (Figures 3(a), (b), (c), and (d)), the formation (roll-up), lift-off, convection, and finally collapse of the cloud cavity (Figure 3(e), (f), (g), and (h)). The re-filling (re-growth) of the sheet cavity takes place at the same time as the cloud cavity is formed and convected downstream, and finally collapses. The volume-fraction distribution and its implied cavitation pattern in Figure 3 are strikingly similar in structure to what some of the photographs in the literature (Kubota *et al*., 1989 [26], 1992 [17]; Foeth *et al*., 2006 [27]) show.

The break-up of the sheet cavity, and the shedding of the cloud cavity can also be visualized with the aid of the span-wise vorticity contour as shown in Figure 4. Note that the snapshots were taken at the same instants of time as in Figure 3. In the vorticity contours shown in Figure 4, the re-entrant jet can be identified as the region of positive span-wise vorticity (red in color) close to the suction side of the hydrofoil surface. Figure 4(a), (b), (c), (d), and (e) clearly show the re-entrant jet progressively penetrating the sheet cavity in the upstream direction all the way to roughly one foil-thickness' distance from the leading-edge, where it finally breaks up the main sheet cavity (Figure 4(e)). The flow, mostly vapor, carrying the vorticity then lifts off from the foil surface, forming the cloud cavity as seen in Figures 3(f) and 4(f). Figure 4(h) together with Figure 3(h) shows a region of high vorticity in the vicinity of the trailing edge where the cloud cavity appears to collapse abruptly. In this respect, our numerical results seem to support what Laberteaux and Ceccio (2001) [28] found in their experimental study with a NACA-0009 hydrofoil. They reasoned that the high vorticity could be due to "baroclinic torque" which arises from the density gradient and the pressure gradient that are not co-linear. It is potentially an important vorticity production mechanism in two-phase flows as indicated by the vorticity transport equation

$$\frac{\partial \boldsymbol{\omega}}{\partial t} + \nabla \times (\boldsymbol{\omega} \times \mathbf{u}) = \frac{1}{\rho^2} \nabla \rho \times \nabla P + \nu \nabla^2 \boldsymbol{\omega} \qquad (20)$$

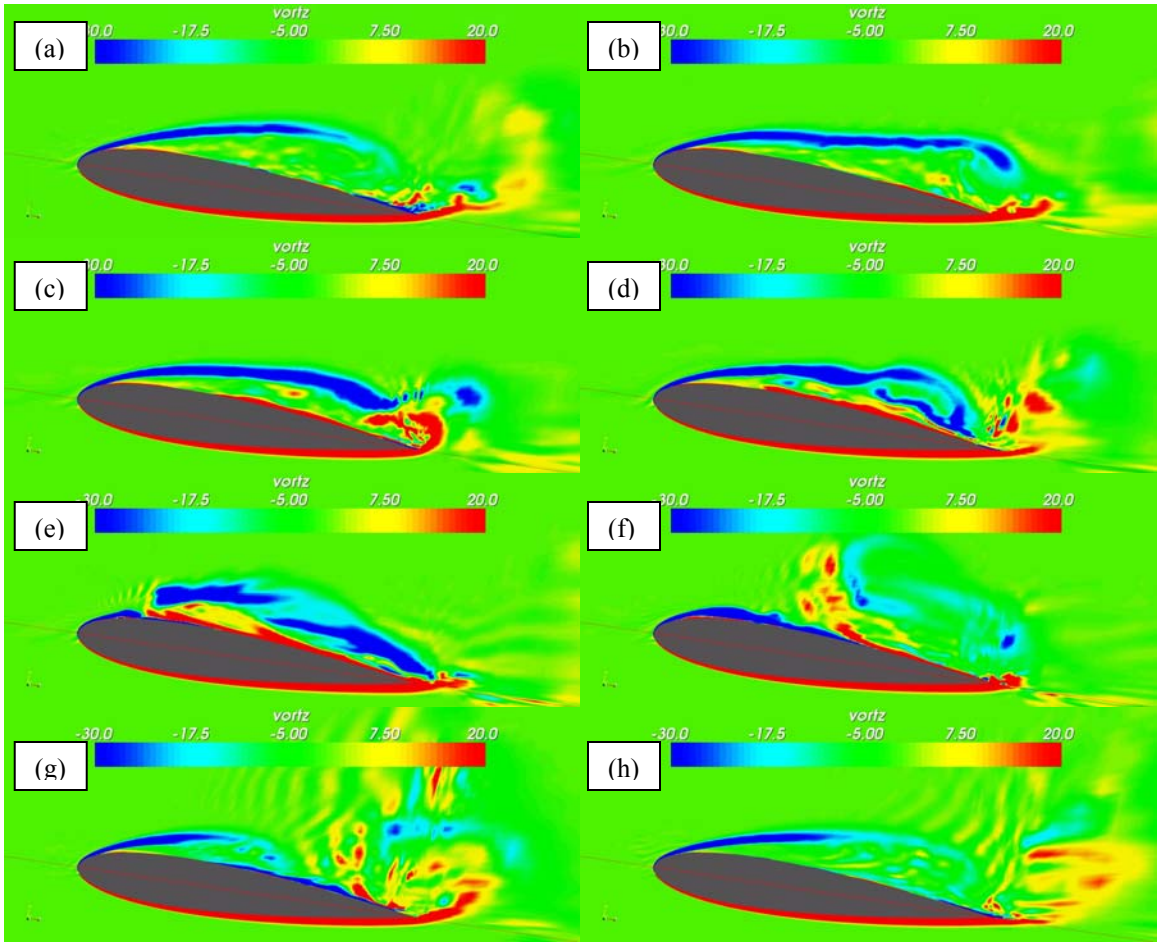

Figure 4. LES (3-D) results - contours of the spanwise vorticity on a longitudinal cut through the mid-span portraying the formaion and shedding of cloud cavity on the NACA-0015 hydrofoil at $\alpha = 8°$ and $\sigma = 1.0$.

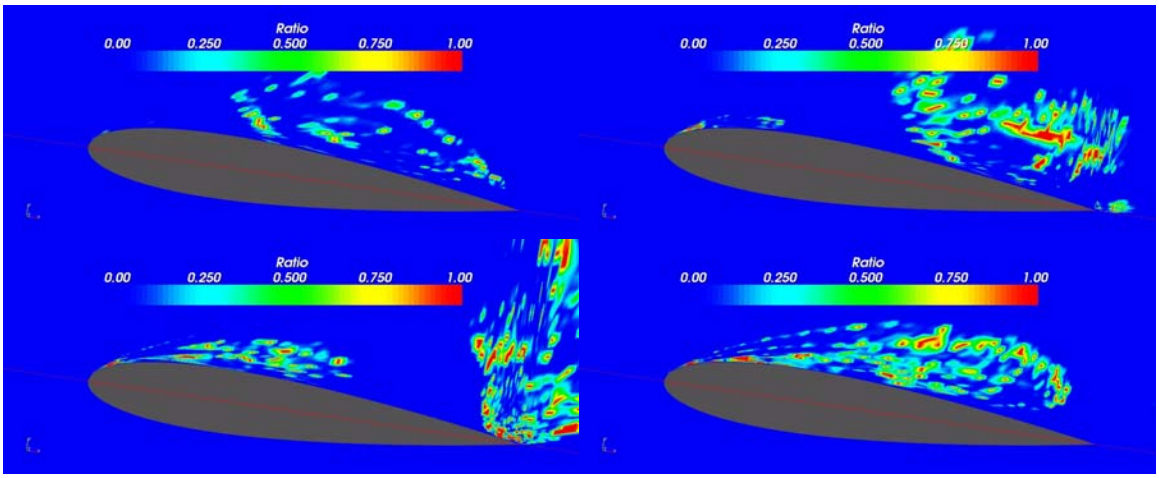

Figure 5. LES (3-D) prediction - contours of the ratio of the baroclinic generation term to the vortex transport /stretching term in (Eq. (21)) on a longitudinal cut through the mid-span on the NACA-0015 hydrofoil at $\alpha = 8°$ and $\sigma = 1.0$.

The second term on the LHS can be expanded to give convection and vortex-stretching/tilting terms. The first term on the RHS represents the barotropic contribution to vorticity production. Obviously, this term vanishes for constant-density or compressible flows with density being a function of pressure only. The production of vorticity via this mechanism can be substantial in cavitating flows as discussed by others (Goplan and Katz, 2000 [29]; Laberteaux and Ceccio, 2001 [28]). To size up the baroclinic contribution for the present flow, the ratio of the baroclinic torque to the transport/stretching term defined by

$$P_{\omega} = \frac{\left|\nabla\rho \times \nabla P\right| / \rho^2}{\left|\nabla \times (\boldsymbol{\omega} \times \mathbf{u})\right|} \qquad (21)$$

was evaluated using the LES results, and four snapshots of its contours are shown in Figure 5. Note that the four snapshots correspond to the last four contour plots in Figures 3 and 4. Indeed, the contribution of the baroclinic torque is significant.

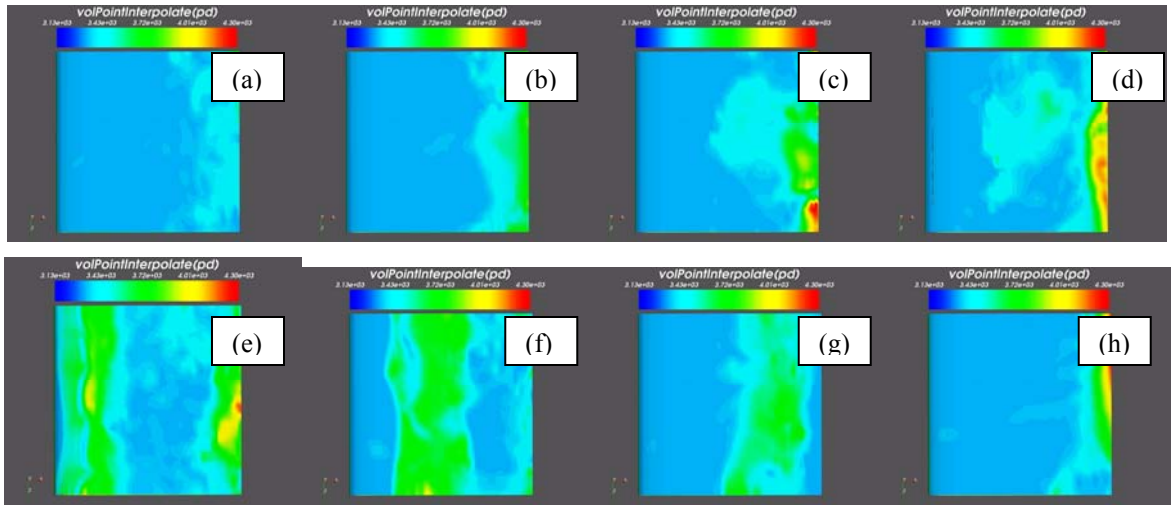

Figure 6. LES (3-D) prediction - contours of instantaneous static pressure on the suction side of the NACA-0015 hydrofoil at $\alpha = 8°$ and $\sigma = 1.0$.

This finding raises a question regarding the adequacy of the cavitation models based on single-phase approaches employing a barotropic relationship between density and pressure, since it would be unable to account for this important contribution. Figure 6 shows the contours of surface pressure on the suction side of the hydrofoil. Figure 7 depicts a perspective view of the sheet/cloud cavitation predicted with the LES computation. Figure 8 shows the results of the DES computations at roughly the same time instants as those in Figure 7. The overall pattern of the cavity such as the oscillation and the break-up of the sheet cavity, the formation

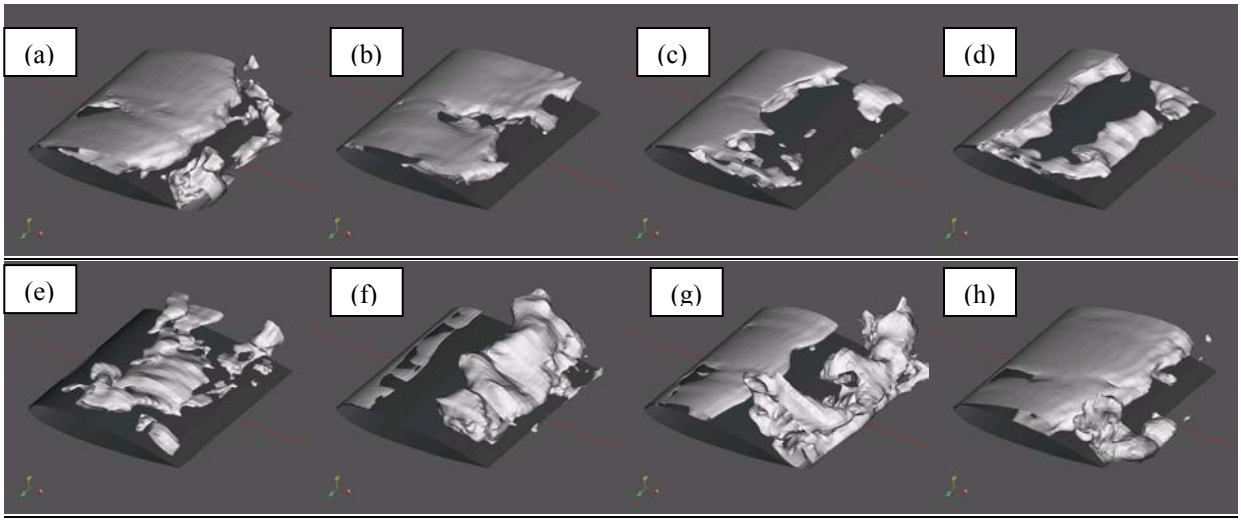

Figure 7. LES prediction - perspective view of the iso-surface of instantaneous volume-fraction (γ = 0.5) illustrating the oscillation of the sheet cavity and the formation and shedding of the cloud cavity on the NACA-0015 hydrofoil at $\alpha = 8°$ and $\sigma = 1.0$.

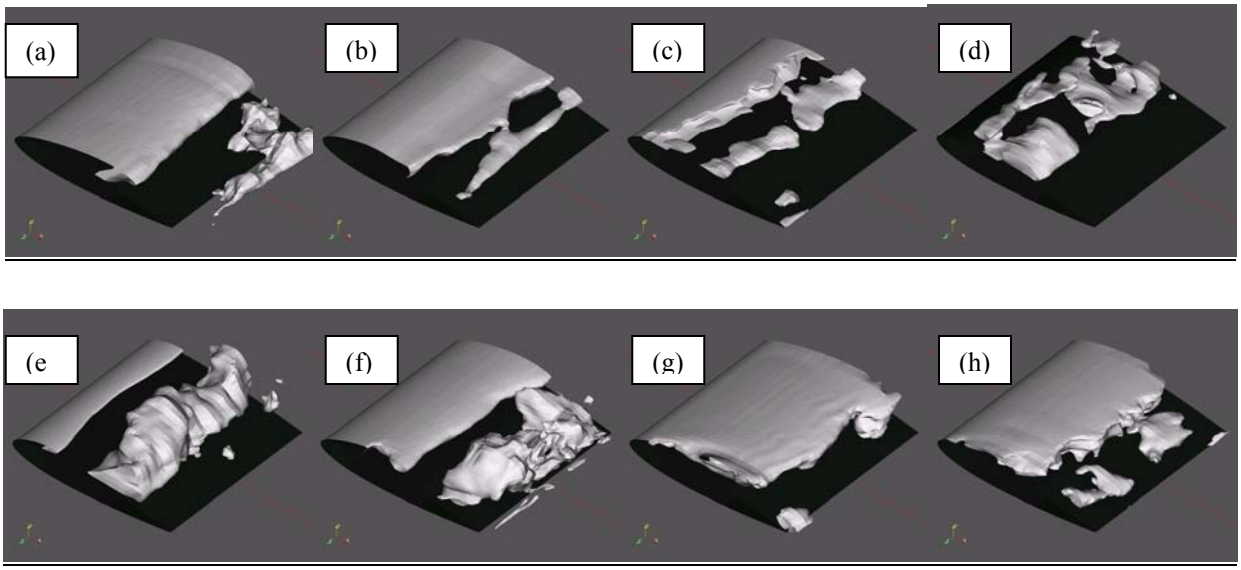

Figure 8. DES prediction - Perspective view of the iso-surface of instantaneous volume-fraction (γ = 0.5) illustrating the oscillation of the sheet cavity and the formation and shedding of the cloud cavity on NACA-0015 hydrofoil at $\alpha = 8°$ and $\sigma = 1.0$.

of the cloud cavity and its shedding and collapse are qualitatively similar to those observed in the LES results.

Unsteady forces on the hydrofoil

The oscillating partial sheet cavity and the shedding of the cloud cavity discussed earlier significantly affect the resulting force and moment on the hydrofoil. Statistics of the fluctuating force and moment such as their mean and root-mean-square values and spectral contents are of major practical concern in naval hydrodynamics, inasmuch as it is the sudden drop-off of lift on hydrofoils and the rapid increase in drag that are responsible for thrust-breakdown in propulsors. Experiments have shown that lift and drag characteristics, namely their mean values and spectral contents, vary with angle of attack and cavitation number (Arndt *et al*., 2001 [15]).

The time-histories of the lift and the drag forces on the NACA-0015 hydrofoil recorded during the RANS, DES, and LES computations are plotted in Figures 9 for $\sigma = 1.0$.

First of all, all the force signals are seen to exhibit periodic behaviors within the time-span during which the force signals were processed. Noteworthy is the finding that the RANS computation for $\sigma = 1.0$ gave considerably different spectral contents from the others, predicting a much lower frequency of the major harmonics than indicated by the LES and the DES results, and the experimental data as well. The force signals from the LES and the DES predictions look quite similar in that they show an identifiable periodicity, that the lift and the drag force signals are well correlated, and that large peaks are seen to periodically occur. Examining the pressure, the volume-fraction, and the vorticity fields together with the force signals, we found that the lift starts dropping as the cloud cavity is formed (rolled up), and hits the minimum around the time when the cloud cavity passes the trailing-edge and is about to collapse, with its time instant roughly coincident with the figure (g) in Figures 3, 4, 6, and 7. Around this time instant, the pressure over a substantial portion of the pressure side toward the trailing edge was found to become quite low, causing a large loss of the lift. Figure 6(g) illustrates what happens to the pressure field. The lift increases again very rapidly after the cloud cavity collapse and as the sheet cavity starts filling the rest of the suction side. By then, the low pressure region around the trailing edge has completely gone. Shortly after that, the lift reaches a peak around the time when the cavity grows to its maximum length and the pressure at the trailing-edge becomes very high as displayed by Figure 6(h).

The primary shedding frequencies of the cloud cavity predicted by LES and DES are shown in Figures 10 for the whole range of cavitation number investigated in this study. The predictions are in excellent agreement with the experimentally observed oscillation frequencies (Arndt *et al.*, 2001 [15]) as shown in the figure. The RANS prediction was not included in this plot. But, as might have been guessed from Figure 9, it was found to give a much lower frequency than the LES and the DES predictions. Between $\sigma = 1.0$ and $\sigma = 1.2$ ($\sigma/2\alpha = 4$), the experimental data indicate that the shedding frequency increases abruptly. This trend is seen to be closely captured by both the LES and the DES predictions.

The time-averaged lift and drag coefficients predicted by the RANS, LES, and DES computations are shown in Figure 11, along with the experimental data measured at $\alpha = 7°$. Note the small difference in the angle of attack between the experiment ($\alpha = 7°$) and the computations ($\alpha = 8°$). The experimental data shown in the figure clearly indicate that the time-averaged lift force (denoted by the black solid line) remains nearly constant as the cavitation number is reduced down to $\sigma = 1.0$, but drops rapidly as the cavitation number is reduced further.

The RANS predictions of the mean C_L and C_D at $\sigma = 1.0$ are significantly lower than those obtained in the experiment. The DES and the LES predictions are shown to capture the trend observed in the experimental – the changes in the lift and the drag forces with the cavitation number. The lift predictions by the LES and the DES alike, denoted in the solid symbols, in Figure 11 are in good agreement with the measurements. The drag predictions, shown in the hollow symbols, came out higher than the experimental data for both the LES and the DES computations. The difference in the angle of attack is considered partly responsible for the discrepancy in the lift and the drag forces. The preliminary result obtained using the finer mesh (3 million cell mesh) did not show any significant changes in the overall levels of the time-averaged lift and the drag forces.

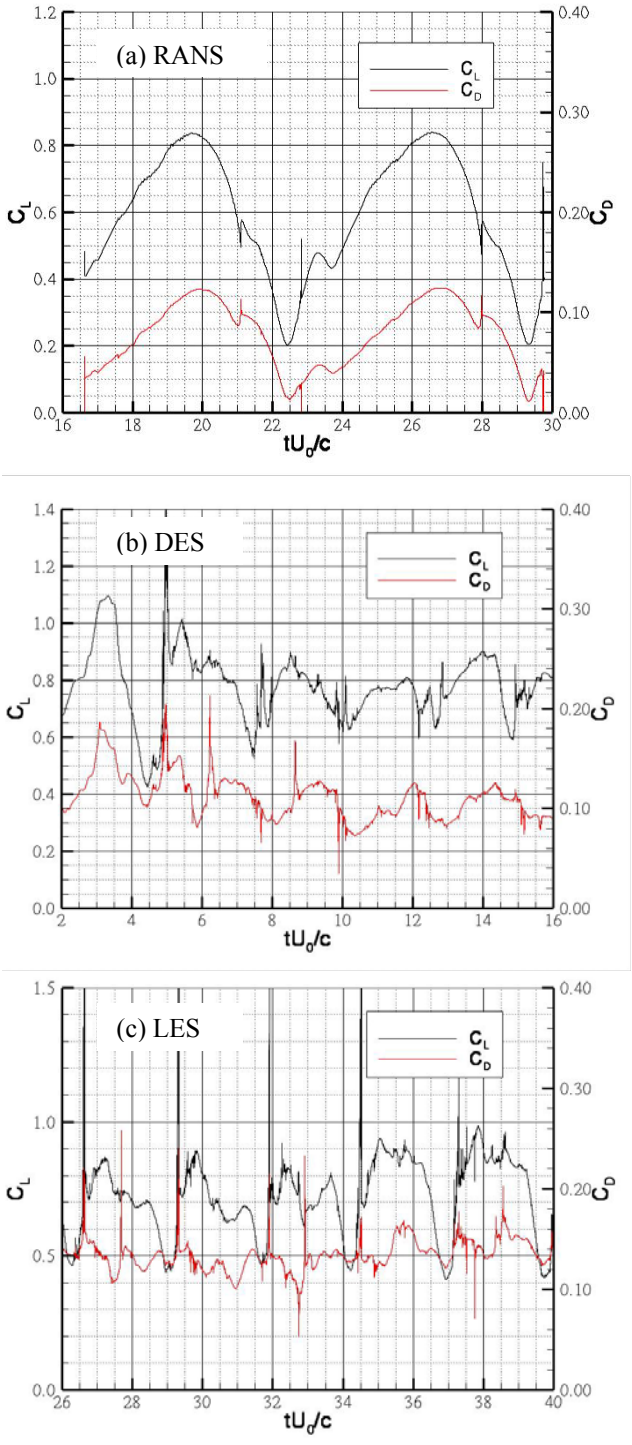

Figure 9. Time histories of lift and drag coefficient at $\alpha = 8°$, $\sigma = 1.0$: (a) RANS; (b) DES; (c) LES.

Figure 12 shows the root-mean-square values of the lift force computed using the signals recorded during the LES and the DES computations. One of the characteristic features of the r.m.s. curve obtained in the experiment is the peak of the r.m.s. C_L occurring around $\sigma = 1.0$ ($\sigma/2\alpha = 3.58$). The LES prediction of the r.m.s. C_L captures the overall trend, although the peak value is somewhat overpredicted, occurring at a slightly lower cavitation index. In the range of higher $\sigma/2\alpha$, the LES and the DES computations severely underpredict the r.m.s. C_L.

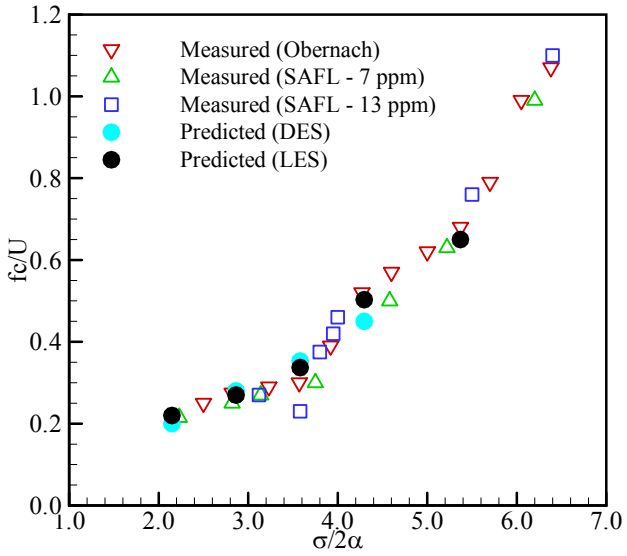

Figure 10. Frequency of cloud cavity shedding and lift oscillation *vs.* the composite index, $\sigma/2\alpha$, observed/measured in the cavitation tunnels - redrawn from Arndt *et al.* (2001) [15].

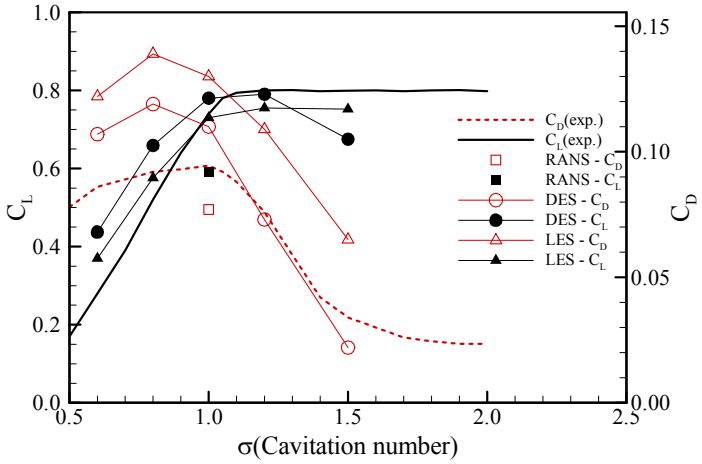

Figure 11. Time-averaged lift and drag coefficients *vs.* σ, measured at α = 7° (redrawn using the data taken from Kjeldsen *et al.*, 2000 [21]).

SUMMARY AND CONCLUSIONS

A multi-phase computational fluid dynamics (MCFD) capability adopting a homogeneous mixture model and a bubble dynamics based phase change model was used to predict the unsteady turbulent cavitating flows on a hydrofoil with finite span and NACA-0015 section. The hydrofoil was selected to assess the performance of the proposed method in predicting complex unsteady cavitating flows involving breakup of sheet cavity by re-entrant jet, and the formation and collapse of cloud cavitation. The computations were made using RANS, LES and DES approaches.

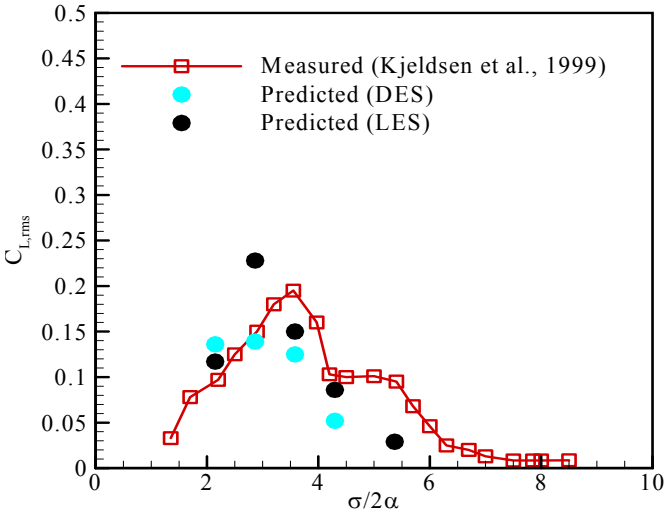

Figure 12. r.m.s. lift fluctuation *vs.* σ, measured at α = 7° (redrawn using the data taken from Kjeldsen *et al.*, 2000 [21]).

The following conclusions were made based on the findings from this study.

- The solution algorithm developed in the course of this study performed quite well for the validation cases for the entire range of the operating conditions investigated in this study.
- The salient features of unsteady three-dimensional cavitation such as the oscillating sheet cavity and the formation and shedding of cloud cavity were reproduced remarkably well by the 3-D unsteady computations using LES and DES. The RANS prediction largely reproduced the main features qualitatively. However, the RANS computation gave poor predictions of the frequency content and the mean values of the lift and drag coefficients.
- LES and DES computations would be needed if the goal is to accurately predict the lift and the drag forces associated with highly unsteady sheet/cloud cavitation on hydrofoils.

ACKNOWLEDGMENT

This work has been financially supported by the Office of Naval Research. The authors would like to thank Dr. Ki-Han Kim, the program manager at the ONR for his support and guidance. We also would like to thank Professor Roger Arndt at the Saint Anthony Falls Laboratory at the University of Minnesota for contributing the figures used in this paper. Also gratefully acknowledged is the technical support from Dr. Henry Weller at OpenCFD Ltd. and Dr. Hrvoje Jasak at Wikki Ltd. with the OpenFOAM software.

REFERENCES

[1] Chahine, G. L., "Nuclei Effects on Cavitation Inception and Noise," *Proceedings of 25th Symposium on Naval Hydrodynamics*, St. John's Newfoundland and Labrador, Canada, 8 – 13, August, 2004.

[2] Merkle, C. L., Feng, J., and Buelow, P. E. O., "Computational Modeling of the Dynamics of Sheet Cavitation," *Proceedings of Third International Symposium on Cavitation*, Grenoble, France, 1998.

[3] Kunz, R. F., Chyczewski, T. S., Boger, D. A., Stinebring, D. R., and Gibeling, H. J.,"Multiphase CFD analysis of Natural and Ventilated Cavitation about Submerged Bodies," *Proceedings of Third ASME/JSME Joints Fluids Engineering Conference* – ASME Paper FEDSM—99-7364, 1999.

[4] Singhal, A. K., Athavale, M. M., Li, H., and Jiang, Y., "Mathematical Basis and Validation of the Full Cavitation Model," *J. Fluid Engineering*, Vol. 124, pp. 617 – 624, 2002.

[5] Senocak, I. and Shyy, W., "A Pressure-Based Method for Turbulent Cavitating Flow Computations," *J Comp Physics* **176**, pp. 363-383, 2002.

[6] Senocak, I. and Shyy, W., "Interfacial Dynamics Based Modeling of Turbulent Cavitating Flows, Part I: Model Development and Steady-State Computations," *Int'l J. Num. Meth. Fluid*, **44**, pp. 975-995, 2004a.

[7] Schnerr, G. H. and Sauer, J., "Physical and Numerical Modeling of Unsteady Cavitation Dynamics," *Proceedings of the 4th International Conference on Multiphase Flows*, New Orleans, L.A., 2001.

[8] Wikstrom, N., Bark, G., Fureby, C., "Large Eddy Simulation of Cavitating Submerged Objects," *Proceedings of the 8th International Conference on Shp Hydrodynamics*, Busan, Korea, September 22 – 25, 2003.

[9] Wikstrom, N., "Modeling of Cavitating Flow Around a Stationary/Moving Wing Profile," AIAA Paper 2005-1287, Presented at the 43rd Aerospace Sciences Meeting & Exhibit, Reno, NV, Jan. 10 – 13, 2005.

[10] Hosangadi, A. and Ahuja, V., "A New Unsteady Model for Dense Cloud Cavitation," FEDSM2005-77485, *Proceedings the ASME Fluids Engineering Division Summer Meeting and Exhibition*, Houston, TX, June 19 – 23, 2005.

[11] Delannoy, Y. and Kueny, J. L., "Two Phase Flow Approach in Unsteady Cavitation Modelling," Cavitation and Multiphase Forum, ASME-FED Vol. 98, pp. 153-158, 1990.

[12] Song, C. C. S. and He, J., "Numerical Simulation of Cavitating Flows by Single-Phase Flow Approach," *Proceedings of 3rd Int'l Symposium on Cavitation*, Vol. 2, pp. 295 – 300, 1998.

[13] Reboud, J. L., Stutz, B., and Coutier, O., "The Two Phase Flow Structure of Cavitation: Experiment and Modeling of Unsteady Effects," *Proceedings of the 3rd Int'l Symposium on Cavitation*, Vol. 2, pp. 203 – 208, 1998.

[14] Coutier-Delgosha, O., Stutz, B., Vabre, A., and Legoupil, S., "Analysis of Cavitating Flow Structure by Experimental and Numerical Investigations," *J. Fluid Mech.*, Vol. 578, pp. 171 – 222, 2007.

[15] Arndt, R. E. A., Song, C. C. S., Kjeldsen, M., and Keller, A., "Instability of Partial Cavitation: A Numerical/Experimental Approach," *Proceedings of the 23rd Symposium on Naval Hydrodynamics*, Val de Reuil, France, Office of Naval Research, National Academic Press, Washington D. C., 2001..

[16] Qin, Q., Song, C. C. S., and Arndt, R. E. A., "Numerical Study of an Unsteady Turbulent Wake Behind a Cavitating Hydrofoil," *Fifth International Symposium on Cavitation* (CAV03-GS-9-001), Osaka, Japan, November 1 – 4, 2003.

[17] Kubota, A., Kato, H., and Yamaguchi, H., "A New Modeling of Cavitating Flows: A Numerical Study of Unsteady Cavitation on a hydrofoil Section," *J. Fluid Mech.*, Vol. 240, pp. 59 – 96, 1992.

[18] Ventikos, Y. and Tzabiras, G., "A Numerical method for the Simulation of Steady and Unsteady Cavitating Flows," *Computers & Fluids*, Vol. 29, pp. 63– 88, 200

[19] Yuan, W. and Schnerr, G. H., "Numerical Simulation of Two-Phase Flow in Injection Nozzles: Interaction of Cavitation and External Jet Formation," *J. Fluid Engineering*, Vol. 125, pp. 963 – 969, 2003.

[20] Wang, G. and Ostoja-Starzewski, M., "Large Eddy Simulation of a Sheet/Cloud Cavitation on a NACA-0015 Hydrofoil," *Applied Mathematical Modeling*, Vol. 31, pp. 417 – 447, 2007.

[21] Kjeldsen, M., Arndt, R. E. A., and Effertz, M., "Spectral Characteristics of Sheet/Cloud Cavitation," *J. Fluid Eng.*, Vol. 122, pp. 481 – 487, 2000.

[22] Ishii, M., *ThermoFluid Dynamic Theory of Two-Phase Flow*, Paris: Eyrolles, 1975.

[23] Wilcox, D.C., *Turbulence Modeling for CFD*, 2nd Edition, DC

[24] Shih, T.-H., Liou, W.W., Shabbir, A., and Zhu, J., "A New k-□ Eddy-Viscosity Model for High Reynolds Number Turbulent Flows - Model Development and Validation," *Computers & Fluids*, Vol. 24, No. 3, pp. 227-238, 1995.

[25] Spalart P.R., Jou W.-H., Strelets M., and Allmaras S.R., "Comments on the feasibility of LES for wings, and on a hybrid RANS/LES approach," 1st AFOSR International Conference on DNS/LES, Aug 4-8 1997, Ruston, LA. In

"Advances in DNS/LES," editors Liu C. and Liu Z., Greyden Press, Columbus OH, 1997.

[26] Kubota, A., Kato, H., and Yamaguchi, H., and Maeda, M., "Unsteady Structures Measurement of Cloud Cavitation on a Foil Section Using Conditional Sampling Technique," *J. Fluids Eng.*, Vol. 111, pp. 204 – 210, 1989.

[27] Foeth, E. J., van Doorne, C. W., H., van Terwisga, T., and Wieneke, B., "Time-Resolved PIV and Flow Visualization of 3D Sheet Cavitation," *Experiments in Fluids*, Vol. 40, pp. 503 – 513, 2006.

[28] Laberteaux, K. R. and Ceccio, S. L., "Partial Cavity Flows- Part I. Cavities Forming on Models Without Spanwise Variation," *J. Fluid Mech.*, Vol. 431, pp. 1 – 41, 2001.

[29] Goplan, S. and Katz, J., "Flow Structure and Modeling Issues in the Closure Region of Attached Cavitation," *Phys. Fluids*, **12**(4), pp. 895, 2000.